



Roll-to-roll fabrication of lithiophilic Sn-modified Cu mesh via chemical tin plating approach for long-cycling lithium metal batteries

Ke-Xin Liu, Ran Tan, Zhong Zheng, Rui-Rui Zhao, Burak Ülgüt*,
Xin-Ping Ai, Jiang-Feng Qian*

Received: 5 March 2024/Revised: 17 April 2024/Accepted: 21 May 2024/Published online: 22 July 2024
© Youke Publishing Co., Ltd. 2024

Abstract Lithium metal, with its exceptionally high theoretical capacity, emerges as the optimal anode choice for high-energy-density rechargeable batteries. Nevertheless, the practical application of lithium metal batteries (LMBs) is constrained by issues such as lithium dendrite growth and low Coulombic efficiency (CE). Herein, a roll-to-roll approach is adopted to prepare meter-scale, lithiophilic Sn-modified Cu mesh (Sn@Cu mesh) as the current collector for long-cycle lithium metal batteries. The two-dimensional (2D) nucleation mechanism on Sn@Cu mesh electrodes promotes a uniform Li flux, facilitating the deposition of Li metal in a large granular morphology. Simultaneously, experimental and computational analyses revealed that the distribution of the electric field in the Cu mesh skeleton induces Li inward growth, thereby generating a uniform, dense composite Li anode. Moreover, the Sn@Cu mesh-Li symmetrical cell demonstrates stable cycling for over 2000 h with an ultra-low 10 mV voltage polarization. In Li||Cu half-cells, the Sn@Cu mesh

electrode demonstrates stable cycling for 100 cycles at a high areal capacity of $5 \text{ mAh}\cdot\text{cm}^{-2}$, achieving a CE of 99.2%. This study introduces a simple and large-scale approach for the production of lithiophilic three-dimensional (3D) current collectors, providing more possibilities for the scalable application of Li metal batteries.

Keywords Roll-to-roll fabrication; Lithiophilic Sn modification; Cu mesh; Li nucleation and growth; Lithium metal batteries

1 Introduction

As the energy density of lithium-ion batteries (LIBs) is approaching its limit, there is currently an emphasis on developing batteries with even higher energy density to meet the growing demands of electric vehicles, smart grids and related fields [1]. Lithium metal anode (LMA) boasts a theoretical specific capacity of $3860 \text{ mAh}\cdot\text{g}^{-1}$ and an exceptionally negative reduction potential of -3.04 V (vs. SHE), making it the preferred anode material for the next generation of rechargeable batteries [2]. Unfortunately, LMA also comes with several fatal drawbacks, such as irregular growth of Li dendrites [3], enormous volume expansion during Li plating/stripping [4], continuous accumulation of dead Li [5] and even safety incidents caused by electrode short-circuiting [6, 7].

Many strategies have been proposed to address these limitations associated with lithium metal, starting from interface modifications, such as tuning the compositions of electrolyte (high-concentration electrolytes (HCE) [8, 9], localized high-concentration electrolytes (LHCE) [10]), constructing protective layers on Li surface (SbF_3 [11], polyvinylidene fluoride (PVDF) [12, 13], covalent-organic

Supplementary Information The online version contains supplementary material available at <https://doi.org/10.1007/s12598-024-02875-7>.

K.-X. Liu, R. Tan, Z. Zheng, R.-R. Zhao, X.-P. Ai, J.-F. Qian*
Hubei Key Laboratory of Electrochemical Power Sources,
College of Chemistry and Molecular Sciences, Wuhan
University, Wuhan 430072, China
e-mail: jfqian@whu.edu.cn

Z. Zheng, R.-R. Zhao
Research Institute, EVE Battery Corporation Limited, Huizhou
516006, China

B. Ülgüt*
Department of Chemistry, Bilkent University, Ankara 06800,
Turkey
e-mail: ulgut@fen.bilkent.edu.tr



framework (COFs) [14, 15]), and designing solid-state electrolytes (Li_3InCl_6 [16], $\text{Li}_7\text{La}_3\text{Zr}_2\text{O}_{12}$ (LLZO) [17], $\text{Li}_7\text{N}_2\text{I}$ [18]). In addition, the shift in current collector morphology from two-dimensional (2D) to three-dimensional (3D) is proved to be a judicious choice [19, 20]. The 3D framework, distinguished by its high porosity, adeptly distributes the current density—an acknowledged factor contributing to lithium dendrite growth is high local current densities [21]. Moreover, the increased specific surface area offers additional nucleation sites for Li deposition [22]. Leveraging these advantages, researchers have designed diverse 3D structures, including carbon materials such as hollow carbons [23, 24], carbon paper [25], carbon nanoballs [26], 3D carbon nanotube sponges (CNTS) [27, 28], and Cu variations such as Cu mesh [29, 30], Cu foam [31, 32] and 3D porous Cu [33]. However, lithiophobicity is a persistent issue that is common for copper-based and carbon-based 3D current collectors, leading to dendrite formation during initial nucleation [34–36].

In order to remedy these limitations, widespread focus has been directed toward understanding Li nucleation and growth [37]. Cui et al. found that the overpotentials of Li are contingent upon the variety of metal substrates [38]. For lithiophobic Cu, the overpotential at $10 \mu\text{A}\cdot\text{cm}^{-2}$ is ~ 40 mV, aimed at overcoming the nucleation barrier arising from the thermodynamic mismatch between Li and Cu lattice. In striking contrast, lithiophilic materials such as Au, Ag and Sn, etc. can form alloy phases with Li and exhibit much lower overpotential [39]. Huang et al. demonstrated that utilizing a carbon fiber substrate decorated with Au as the current collector enhances efficient spatial utilization within the 3D structure, promoting a consistent and compact deposition of Li metal from bottom to top [40]. However, most carbon-based current collectors necessitate prolonged production times, which can be cumbersome. In contrast, leveraging contemporary technological capabilities, copper-based current collectors, which can be commercialized more swiftly, are increasingly preferred for their efficiency and practicality [41, 42]. Xie et al. developed that 3D Cu foam modified with Ag nanoparticles (Cu@Ag) reduces the nucleation overpotential for Li, resulting in excellent battery performance for over 1200 h at a current density of $1 \text{ mA}\cdot\text{cm}^{-2}$ and a capacity of $1 \text{ mAh}\cdot\text{cm}^{-2}$ [43]. Nonetheless, the prohibitive costs associated with Au and Ag hinder their practical implementation. Wang et al. employed an electrochemical approach to fabricate Sn@Cu mesh [44]. This cost-effective material offers additional electrochemical active sites, reducing the nucleation overpotential of Li on the Cu substrate. However, the time-consuming and energy-intensive nature hinders its large-scale application.

In this work, the roll-to-roll method was utilized to fabricate meter-sized Cu mesh modified with Sn (Sn@Cu

mesh). Simultaneously, the addition of Sn resolves the wetting issue between Cu and Li, inducing the 2D growth of Li and promoting a more uniform Li deposition behavior. In contrast, the bare Cu mesh substrate exhibits uneven deposition of Li due to its high nucleation overpotential and irregular flow of Li (Fig. 1a). Benefiting from the synergistic effect of lithiophilic Sn and the high porosity of Cu mesh, the Sn@Cu mesh exhibited high electrochemical reversibility for 100 cycles at a current density of $1 \text{ mA}\cdot\text{cm}^{-2}$ and a capacity of $5 \text{ mAh}\cdot\text{cm}^{-2}$ with the Coulombic efficiency (CE) exceeding 99.2%. Especially, no short circuits of Sn@Cu mesh-Li||Sn@Cu mesh-Li cells occur even after cycling for over 2000 h at an ultra-low polarization of 10 mV under a current density of $1 \text{ mA}\cdot\text{cm}^{-2}$ up to a capacity of $1 \text{ mAh}\cdot\text{cm}^{-2}$. Furthermore, in N/P = 0 (the capacity ratio between the negative electrode and the positive electrode) pouch cells (Sn@Cu mesh||LiNi_{0.5}Co_{0.2}Mn_{0.3}O₂), the Sn@Cu mesh electrode continues to demonstrate excellent cycling stability, surpassing that of the bare Cu mesh by a wide margin.

2 Experimental

2.1 Materials

All reagents and solvents were provided by Aladdin Company and used without further purification. Li metal chips were obtained from Guangdong Canrd New Energy Technology Co., Ltd. (1 mm in thickness, 15.6 mm in diameter) Commercial Cu mesh (300 meshes, with 50 μm diameter wires spaced at 80 μm intervals) was purchased from Colleague Hardware Co. The electrolyte solution, of battery-grade quality, was supplied by Duodu Chemicals (Suzhou, China). High-loading LiFePO₄ and LiNi_{0.5}Co_{0.2}Mn_{0.3}O₂ cathode sheets (LiFePO₄ (LFP): $12 \text{ mg}\cdot\text{cm}^{-2}$, single side LiNi_{0.5}Co_{0.2}Mn_{0.3}O₂ (NCM523): $10 \text{ mg}\cdot\text{cm}^{-2}$, and double side NCM523: $23.1 \text{ mg}\cdot\text{cm}^{-2}$) were provided by Shenzhen KeJing Star Technology Co., Ltd.

2.2 Fabrication of Sn@Cu mesh

The chemical Sn-plating solution was prepared by dissolving 0.1 M stannous chloride dihydrate ($\text{SnCl}_2\cdot 2\text{H}_2\text{O}$), 0.07 M trisodium citrate dihydrate ($\text{C}_6\text{H}_5\text{Na}_3\text{O}_7\cdot 2\text{H}_2\text{O}$), 0.7 M sodium hypophosphite (NaH_2PO_2), 1.2 M thiourea ($\text{CH}_4\text{N}_2\text{S}$), 8.0 mL 37% HCl, and 6.0 mL OP-10 in 240 mL distilled water at 60 °C. Then, a 1 m length of commercial Cu mesh was immersed in the Sn-plating solution for reaction durations of 3, 5, 10 and 15 s, respectively.

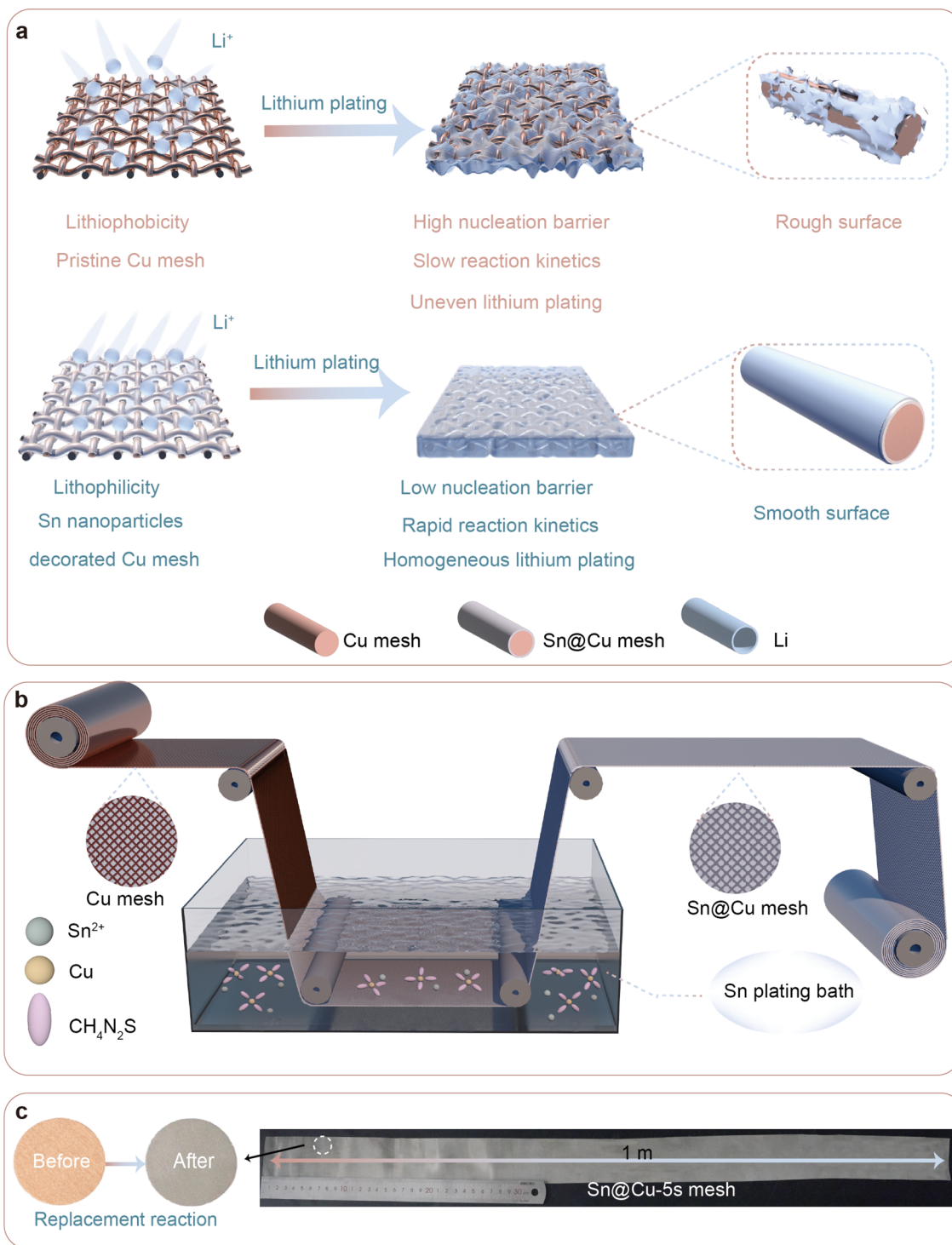


Fig. 1 **a** Schematic configuration of Li plating process on Cu mesh and Sn@Cu mesh skeleton; **b** schematic illustration of roll-to-roll device for chemical Sn plating on Cu mesh; **c** optical photograph of 1 m-long Sn@Cu mesh prepared under laboratory conditions

2.3 Structure and morphology characterizations

X-ray diffraction (XRD) analysis was performed on Cu mesh and Sn@Cu mesh using the Rigaku SmartLab SE

instrument. Cu K α radiation was utilized with a scanning speed of 4 (°)·min⁻¹, ranging from 10° to 80°. X-ray photoelectron spectroscopy (XPS) was employed to analyze the surface structures of Cu mesh and Sn@Cu mesh,

utilizing monochromatic Al K α radiation (225 W, 15 mA, 15 kV). For Scanning Electron Microscopy (SEM) measurements, cycled cells were disassembled within a glove box to retrieve the desired Cu mesh and Sn@Cu mesh electrodes. These sheets were carefully cleaned using 2 mL anhydrous dimethyl ether solvent to remove any remaining electrolytes and salts. Subsequently, they are subjected to vacuum drying and then sealed in a container inside the glovebox. The morphology of Li deposition on Cu mesh and Sn@Cu mesh was revealed by SEM using Zeiss Merlin Compact. The elemental distribution of Cu mesh and Sn@Cu mesh was analyzed using Energy Dispersive X-ray Spectroscopy (EDS) attached to SEM (X-MaxN, Oxford Instruments).

2.4 Electrochemical measurements

The electrochemical tests were conducted using CR2032 coin cells assembled in a glovebox filled with argon ($O_2 < 0.1$ ppm, $H_2O < 0.1$ ppm). The electrolyte for only the M/M-Li||NCM523 (M = Cu mesh, Sn@Cu mesh) battery was $1.0 \text{ mol}\cdot\text{L}^{-1}$ LiPF $_6$ dissolved in ethylene carbonate/dimethyl carbonate/ethyl methyl carbonate (EC/DMC/EMC, 1:1:1 in vol%) while the electrolyte for all other batteries was $1.0 \text{ mol}\cdot\text{L}^{-1}$ LiTFSI dissolved in 1,3-Dioxolane /1,2-Dimethoxyethane (DOL/DME, 1:1 in vol%) with 2 wt% lithium nitrate (LiNO $_3$). The separator for all batteries was Celgard 2320. The constant current charge–discharge performance was evaluated using the LAND-CT 2001A multi-channel battery tester (Land, China). Li||M half cells underwent cycling at a fixed capacity of 1 and 5 mAh·cm $^{-2}$, employing current densities of 0.5, 1 and 2 mA·cm $^{-2}$, with Li metal plated to achieve the designated capacity. The cells were discharged to 0.2 V. M-Li||M-Li (M-Li: Pre-deposition of 10 mAh·cm $^{-2}$ Li on Cu mesh/Sn@Cu mesh electrodes) symmetric batteries were employed for constant current testing at the capacity of 1 mAh·cm $^{-2}$ and the current density ranging from 0.5 to 4 mA·cm $^{-2}$. For M-Li||LFP full batteries (the capacity ratio between the negative electrode and the positive electrode, N/P = 5.6), M-Li was paired with 12 mg·cm $^{-2}$ LFP, and the charge–discharge cycles were conducted at 0.5C within the voltage range of 2.5–3.8 V. The M||LFP anode-free Li metal batteries (N/P = 0) were cycled under conditions of 0.5C at 3–3.8 V. Charging and discharging current density for the M-Li||NCM523 (single side NCM523: 10 mg·cm $^{-2}$, N/P = 6.25) battery was 1C, with a voltage range of 2.5–4.3 V. Additionally, for pouch cell, the Cu mesh/Sn@Cu mesh were paired with double-sided NCM523 loading at 23.1 mg·cm $^{-2}$. The electrodes were within the shape of 5.0 cm \times 5.5 cm. Cyclic voltammetry (CV) experiments were conducted using the Ivium-n-Stat electrochemical workstation at scan rates of 0.1 and 5 mV·s $^{-1}$.

Tafel plots were obtained within the range of -0.1 to 0.1 V at $0.1 \text{ mV}\cdot\text{s}^{-1}$. The battery underwent discharge to 0 V and was held at this potential for a specific duration, followed by constant voltage testing at -0.01 V. Electrochemical impedance spectroscopy (EIS) measurements were performed on Admiral electrochemical workstation, covering a frequency range of 1×10^{-2} to 1×10^5 Hz with an amplitude of 10 mV.

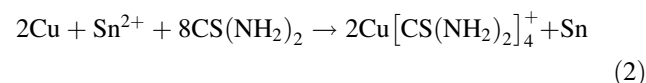
2.5 Computational details

To simulate the distribution of electric field intensity around the copper mesh, a 2D geometric model was established. In this model, several circular shapes represent the cross-section of the copper, and the surrounding area of the mesh is filled with a 1.0 M LiPF $_6$ in EC: DEC (1:1 in vol%) electrolyte solution. A higher electrical potential was set at the upper boundary of the model. The model was constructed in COMSOL Multiphysics 6.0 and a steady-state simulation was carried out using the electrostatic physics field.

3 Results and discussion

3.1 Preparation and characterization of Sn@Cu mesh

The Sn@Cu mesh is prepared through a simple one-step chemical displacement reaction involving Cu and Sn $^{2+}$. The specific reactions and equations are as follows:



$$E^\theta = \varphi_+^\theta - \varphi_-^\theta \quad (3)$$

$$\Delta G^\theta = -zE^\theta F \quad (4)$$

where E^θ is standard electrode potential, φ_+^θ and φ_-^θ are the standard reduction potential of the positive and negative electrode, respectively, ΔG^θ is the standard Gibbs free energy, z is the stoichiometric number of electrons, and F is Faraday constant.

However, it is known that the standard electrode potential for Cu ($\varphi(\text{Cu}^+/\text{Cu}) = 0.512$ V (vs. SHE) [44] and Sn ($\varphi(\text{Sn}^{2+}/\text{Sn}) = -0.138$ V (vs. SHE)) [45], based on Eqs. (1, 2), results in ΔG^θ for Reaction (1) being $74.0 \text{ kJ}\cdot\text{mol}^{-1} > 0$. Therefore, thermodynamically, this reaction cannot occur spontaneously. Interestingly, by introducing thiourea ($\text{CS}(\text{NH}_2)_2$) as a strong chelating agent for Cu^+ into the Sn plating solution, the Cu electrode potential can be reduced to $\varphi(\text{Cu}[\text{CS}(\text{NH}_2)_2]_4^+/\text{Cu}) = -0.399$ V (vs. SHE). As the

Reaction (2), the calculated ΔG for Reaction (2) is $-50.5 \text{ kJ}\cdot\text{mol}^{-1} < 0$. This means that the reaction can occur spontaneously, ultimately leading to the replacement reaction between metallic Sn and Cu.

The raw Cu mesh exhibits a purplish Cu hue, which changes to a bright silver-white tone after a brief immersion in the Sn solution for 5 s, denoted as Sn@Cu-5s mesh. Moreover, benefiting from the straightforward scalability of the solution reaction, we successfully fabricated a one-meter-long Sn@Cu mesh using a roll-to-roll method under laboratory conditions. (Figs. 1b, c, S1) To examine the phase structure of the modified current collector, XRD was performed on Cu and Sn@Cu-5s meshes. From Figs. 2a, S2, it is evident that both meshes exhibit distinct peaks belonging to (111), (200) and (220) planes of Cu (JCPDS No. 04-0836). Additionally, weak characteristic peaks of Sn (JCPDS No. 04-0673) are observed at 30.36° , 31.82° and 44.65° for Sn@Cu-5s mesh, manifesting a successful Sn substitution reaction occurring on the Cu surface. Moreover, a faint peak of Cu_6Sn_5 (JCPDS No. 45-1488) observed at 29.98° (Fig. S2) confirms the close contact between the Cu mesh substrate and Sn particles, forming a trace of Cu_6Sn_5 alloy [46].

XPS analysis was further conducted to determine the chemical composition of Sn@Cu-5s mesh. As shown in Fig. 2b, distinct Sn $3d_{3/2}$ and Sn $3d_{1/2}$ characteristic peaks are observed in Sn@Cu-5s mesh [47], confirming the presence of Sn layer. The Cu 2p spectrum is shown in Fig. 2c. The peaks at 932.09 and 951.87 eV correspond to Cu $2p_{3/2}$ and Cu $2p_{1/2}$ of metallic Cu^0 , while shoulder peaks at 934.18 and 954.08 eV correspond to Cu^{2+} of copper oxides [48]. This signifies the existence of a copper oxide layer on the pristine Cu mesh. In contrast, the Sn@Cu-5s mesh exclusively exhibits Cu $2p_{3/2}$ and Cu $2p_{1/2}$ peaks of Cu^0 , with no noticeable appearance of Cu^{2+} characteristic peaks, suggesting that the modification with the Sn layer prevents secondary oxidation of the Cu mesh.

The microscopic morphology of the samples was analyzed using scanning electron microscopy (SEM). As shown in Fig. 2d–f, the Cu mesh is intricately woven from 50- μm -diameter wires spaced at 80 μm intervals, forming a porous skeleton. This structure contributes to a porosity of 50% and has a theoretical Li storage capacity of up to 5 $\text{mAh}\cdot\text{cm}^{-2}$. The surface of the pristine Cu mesh is relatively smooth, while the Sn@Cu-5s mesh (Fig. 2g–i) is covered by a layer of Sn nanoparticles. Cross-sectional SEM images of a single Cu wire and corresponding EDS images (Fig. 2j–l) illustrate that the Sn layer tightly encapsulates the Cu wire with a uniform thickness of 500 nm. The even distribution of Sn will serve as the foundation for uniform Li deposition in subsequent processes. Moreover, these findings indicate that the chemical

Sn plating method has successfully generated an ultra-thin and uniform Sn layer on the Cu mesh.

In addition, it is crucial to note that the Sn-plating time has a direct impact on the uniformity and thickness of the Sn coating layer, as well as the subsequent electrochemical performance of Li metal deposition. As demonstrated in Fig. S3, a short Sn-plating time of only 3 s results in incomplete coverage of the Cu mesh, which is unfavorable for the uniform Li nucleation. Conversely, as the Sn-plating time is extended to 10 and 15 s (Figs. S4, S5), the Sn layer thickness is continuously increased to 1 and 2 μm , respectively, accompanied by an escalating presence of cracks and pinholes in the Sn layer. These excessively thick Sn, as observed in the 10 and 15 s cases, would cause significant volume expansion during the Li–Sn alloying/dealloying processes, adversely affecting the Li plating stability over prolonged periods [49]. Furthermore, CE tests (Fig. S6) on the Sn@Cu-0s, Sn@Cu-3s, Sn@Cu-5s, Sn@Cu-10s and Sn@Cu-15s meshes confirm that the Sn@Cu-5s sample exhibits the best Li deposition/stripping stability, sustaining over > 280 cycles with an average CE of 98.6%. However, too thin or thick Sn coatings compromise its regulatory role for stable Li nucleation. Therefore, Sn@Cu-5s mesh is identified as the optimal Sn-plating time, and this sample will be referred to as Sn@Cu mesh for simplicity in the subsequent text unless otherwise specified.

3.2 Lithiophilic property of Sn decorating layer

The wetting tests of molten Li on Cu meshes are illustrated in Fig. 3a, b. The contact angle between Li and the Cu mesh is nearly non-wetting, measuring 139.5° . In contrast, on the surface of Sn@Cu mesh, molten Li spontaneously spreads out, exhibiting a significantly reduced contact angle of only 20.5° . Overpotential (η) is also a typical parameter for lithiophilicity assessment, defined as the voltage difference between the initial drop and subsequent plateau, as shown in Eq. (5) [38]. Figure 3c and Table S1 illustrate the overpotential (η) of Li on the Cu mesh as 40 mV, which is coincident with the work of Cu current collector reported in previous studies [44]. Surprisingly, the overpotential of Sn@Cu mesh is merely 4 mV, a ten-fold reduction compared to Cu mesh, confirming its remarkable lithiophilicity. The pronounced lithiophilicity of the Sn layer stems from the formation of a Li–Sn solid solution [50, 51]. To investigate the formation of Li–Sn alloy, as shown in Fig. 3d, CV curve of Sn@Cu mesh electrode was tested in the voltage range of 0–1.5 V at the scan rate of $0.1 \text{ mV}\cdot\text{s}^{-1}$. During cathodic scanning at 0.67, 0.52 and 0.37 V, three distinctive reduction peaks were observed, corresponding to the formation of LiSn, Li_7Sn_3 and $\text{Li}_{22}\text{Sn}_5$ [52], as depicted in Reaction (3). The

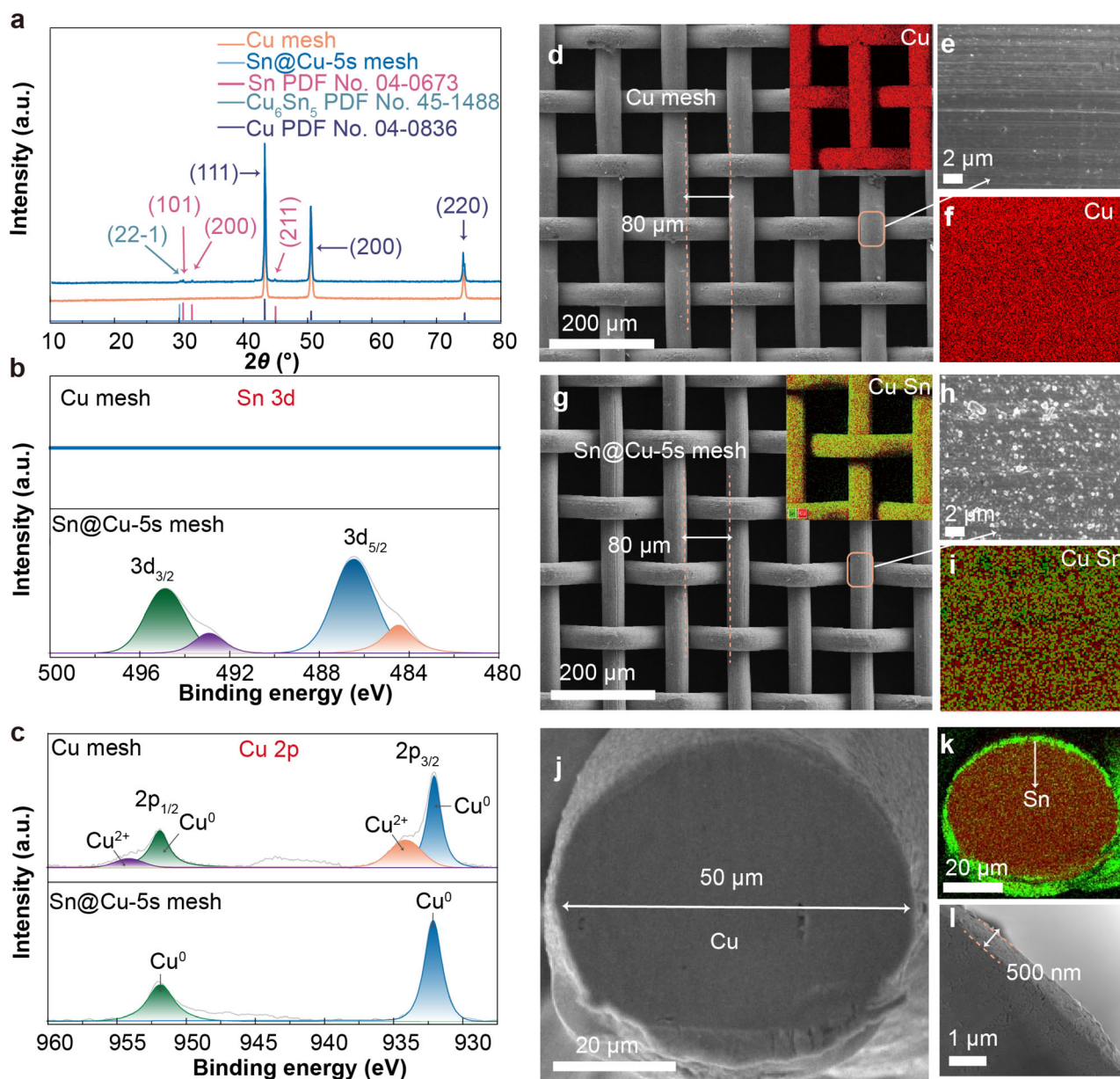


Fig. 2 a XRD patterns and b, c XPS spectra of Cu mesh and Sn@Cu-5s mesh; SEM images and EDS map of d–f Cu mesh and g–i Sn@Cu-5s mesh; j–l SEM image and EDS map of a single Cu wire modified with Sn coating layer

appearance of a reduction peak at 0.14 V suggests a potential transformation-alloying reaction, possibly resulting in the generation of Cu and $\text{Li}_{22}\text{Sn}_5$ through the conversion of Cu_6Sn_5 [53], consistent with XRD results (Fig. 2a). Additionally, four oxidation peaks at 0.48, 0.63, 0.73 and 0.81 V correspond to the Li–Sn dealloying process. Meanwhile, the CV curves of the Sn@Cu mesh electrode exhibit consistent heights over three consecutive scans, confirming the ability of the Sn layer to maintain excellent reversibility during repeated cycles. Subsequently, LillCu mesh and LillSn@Cu mesh batteries were

utilized to explore the reaction kinetics of Li plating/stripping behavior. As depicted in Fig. 3e, f, the CV curves and Tafel plots of LillCu mesh and LillSn@Cu mesh batteries reveal that the Sn@Cu mesh exhibits a significantly higher exchange current density ($21.2 \text{ mA}\cdot\text{cm}^{-2}$) than the Cu mesh ($7.63 \text{ mA}\cdot\text{cm}^{-2}$). The modification of the ultra-thin Sn layer enhances the charge transfer kinetics of the electrode, thereby promoting the dispersion of Li nucleus on the electrode surface the electrode, which is beneficial for achieving uniform Li deposition [54, 55].

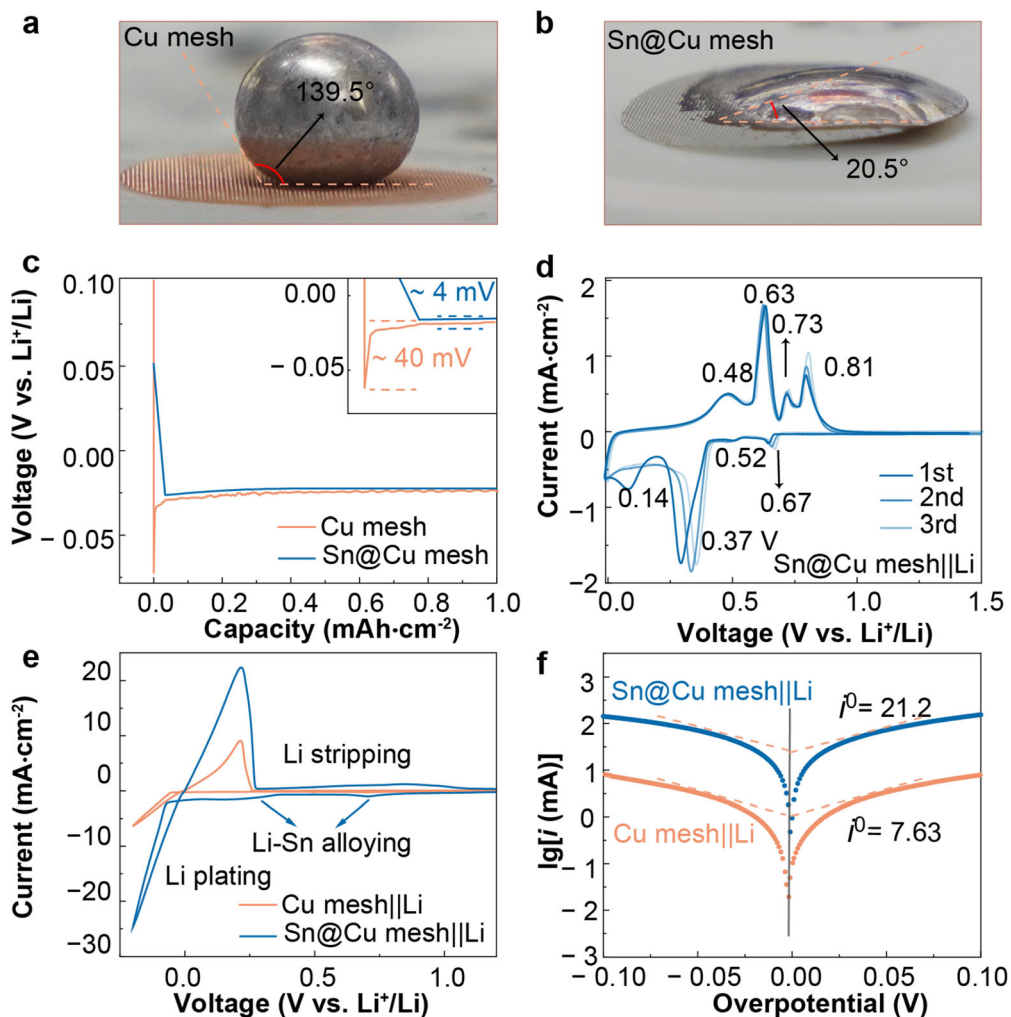
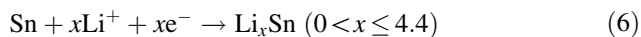


Fig. 3 Digital photos of **a** bare Cu mesh and **b** Sn@Cu mesh; **c** galvanostatic discharge voltage curve of Li deposition process at $0.5 \text{ mA}\cdot\text{cm}^{-2}$; **d** CV curves of Sn@Cu mesh anode between 0 and 1.5 V at a scan rate of $0.1 \text{ mV}\cdot\text{s}^{-1}$; **e** CV curves of Cu mesh and Sn@Cu mesh electrode within potential range of -0.2 to 0.5 V at scanning rate of $5 \text{ mV}\cdot\text{s}^{-1}$ (Li metal disks: counter and reference electrodes for CV tests); **f** Tafel curves of Cu mesh and Sn@Cu mesh electrodes

$$\eta = |\eta_n| - |\eta_m| \quad (5)$$

where η_n is nucleation overpotential, η_m is minimum overpotential.



3.3 Characterizations of Li plating behavior on Sn@Cu mesh

SEM was utilized to delineate the nucleation and growth processes of Li metal on the frameworks of both Cu mesh and Sn@Cu mesh. The deposition morphology of $0.5 \text{ mAh}\cdot\text{cm}^{-2}$ Li on Cu mesh is illustrated in Fig. 4a, predominantly featuring small Li grains. As the deposition capacity increases, the small grain Li evolves into fibrous dendrites with diameters of $\sim 1\text{--}2 \mu\text{m}$. Even at the deposition capacity of $10.0 \text{ mAh}\cdot\text{cm}^{-2}$, a significant

presence of Li dendrites can be observed, occupying the pores (Figs. 4b, c, S9a–d). In the cross-sectional view of Fig. 4d, it can be observed that loosely porous Li is deposited on the Cu mesh substrate, leading to hindered ion–electron connectivity, thereby impeding the mass transport processes and significantly increasing internal resistance. In stark contrast, at a deposition capacity of $0.5 \text{ mAh}\cdot\text{cm}^{-2}$, we speculate that this phenomenon may be attributed to the divergent nucleation mechanisms of Li on the Sn@Cu mesh electrode compared to the Cu mesh. When the deposition capacity reaches 1.0 and $2.0 \text{ mAh}\cdot\text{cm}^{-2}$ (Figs. 4f, S10a), the inward growth of large Li particles occurs within the Sn@Cu mesh. Upon reaching $5.0 \text{ mAh}\cdot\text{cm}^{-2}$ (Figs. 4g, h, S10b, c), the pores of the Sn@Cu mesh are nearly filled with Li, consistent with the theoretical pore volume. COMSOL simulations (Fig. 4i) further corroborate the preferential growth of Li occurring

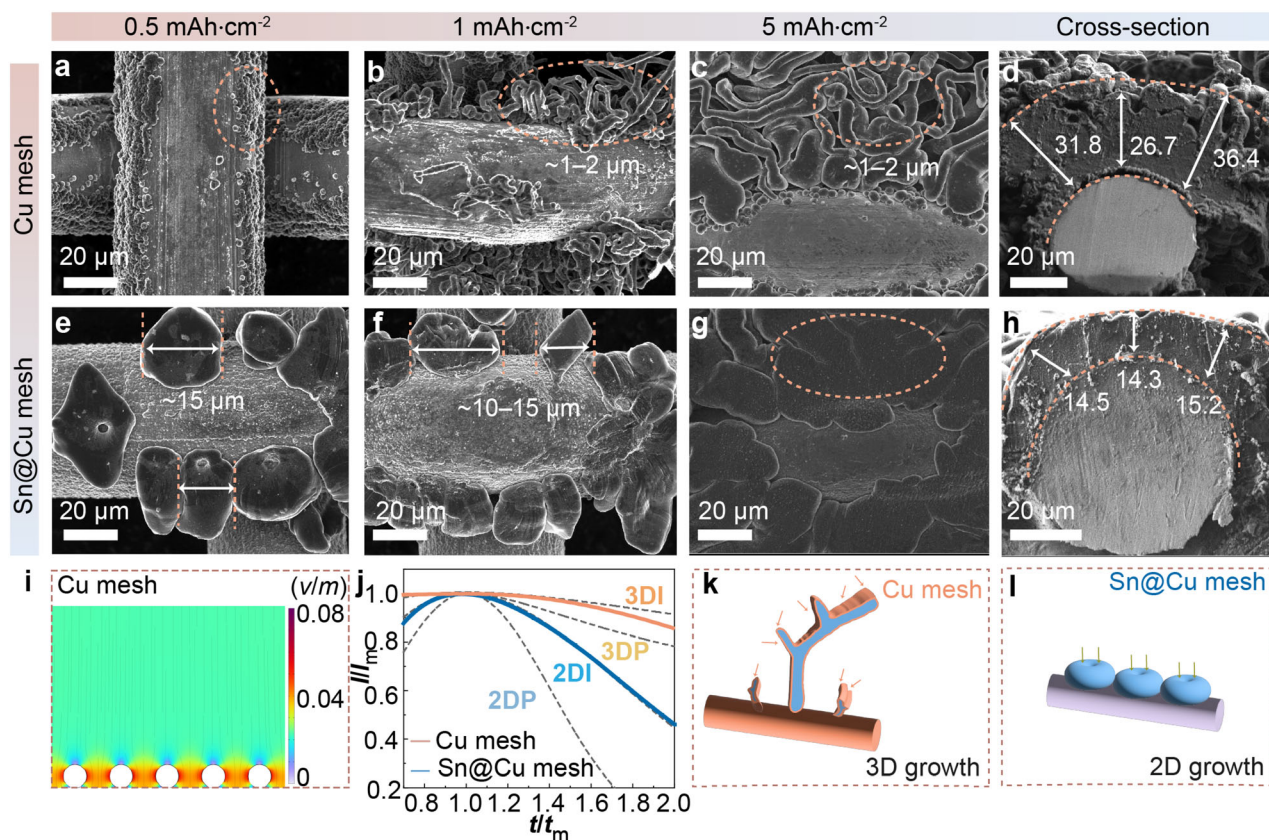


Fig. 4 SEM images of Li deposition on Cu mesh anode at **a** $0.5 \text{ mA}\cdot\text{cm}^{-2}$, **b** $1 \text{ mA}\cdot\text{cm}^{-2}$, **c** $5 \text{ mA}\cdot\text{cm}^{-2}$ and **d** cross section at $5 \text{ mA}\cdot\text{cm}^{-2}$; microscope images of Sn@Cu mesh anode at Li plating amount of **e** $0.5 \text{ mA}\cdot\text{cm}^{-2}$, **f** $1 \text{ mA}\cdot\text{cm}^{-2}$, **g** $5 \text{ mA}\cdot\text{cm}^{-2}$ and **h** cross-section of **g**, **i** electric field distribution of Cu mesh; **j** plots of t/t_m and $(I/I_m)^2$ with theoretical 2D and 3D models for Li||Cu mesh and Li||Sn@Cu mesh; schematic diagrams of **k** 3D and **l** 2D nucleation (all Li plating processes were carried out under current density of $0.5 \text{ mA}\cdot\text{cm}^{-2}$)

within the pore structures [56]. Moreover, an increase to $10.0 \text{ mA}\cdot\text{cm}^{-2}$ leads to the complete encapsulation of the Sn@Cu mesh by a uniform, dense layer of Li metal (Fig. S10d).

The constant potential method is a valuable experimental tool for studying Li nucleation and growth behavior [57]. Through non-dimensional analysis, we obtain I/I_m (the ratio of instantaneous current to peak current) versus t/t_m (the ratio of time to the time needed to achieve the peak current) plots, fitting them to theoretical formulas for 2D or 3D growth mechanisms and progressive (P) or instantaneous (I) nucleation (Table S2) for both Cu mesh and Sn@Cu mesh electrodes [58]. The nucleation of Li on the bare Cu mesh tends to be 3D, as shown in Fig. 4j. The growth of Li is controlled by volume diffusion [59], resulting in significant Li^+ concentration gradients. Over time, the high surface area of Li dendrites will be facilitated by the 3D growth of Li perpendicular to the substrate (Fig. 4k), leading to uneven Li deposition. This growth behavior aligns with the Volmer-Weber growth model,

which describes situations where the interaction between the same metals is stronger than the interaction between metal and substrate [60]. In comparison, Li nucleation on Sn@Cu mesh aligns more closely with 2D growth, providing a perfect validation of our conjecture. At this point, Li growth is controlled by surface diffusion [61], ensuring a more uniform Li flux and causing Li to grow along the substrate plane (Fig. 4l). The result indicates that the interaction between the metal and the substrate is stronger than the interaction between identical metals, and is more consistent with the Frank-van der Merwe growth model [25]. This finding confirms the regulatory role of Sn in the nucleation and growth of Li.

3.4 Electrochemical performance of Sn@Cu mesh

CE is regarded as an important metric for evaluating the sustainability of Li deposition/stripping processes (Figs. S11, S12). The Sn@Cu mesh electrode demonstrates remarkable stability, with an average Coulombic efficiency

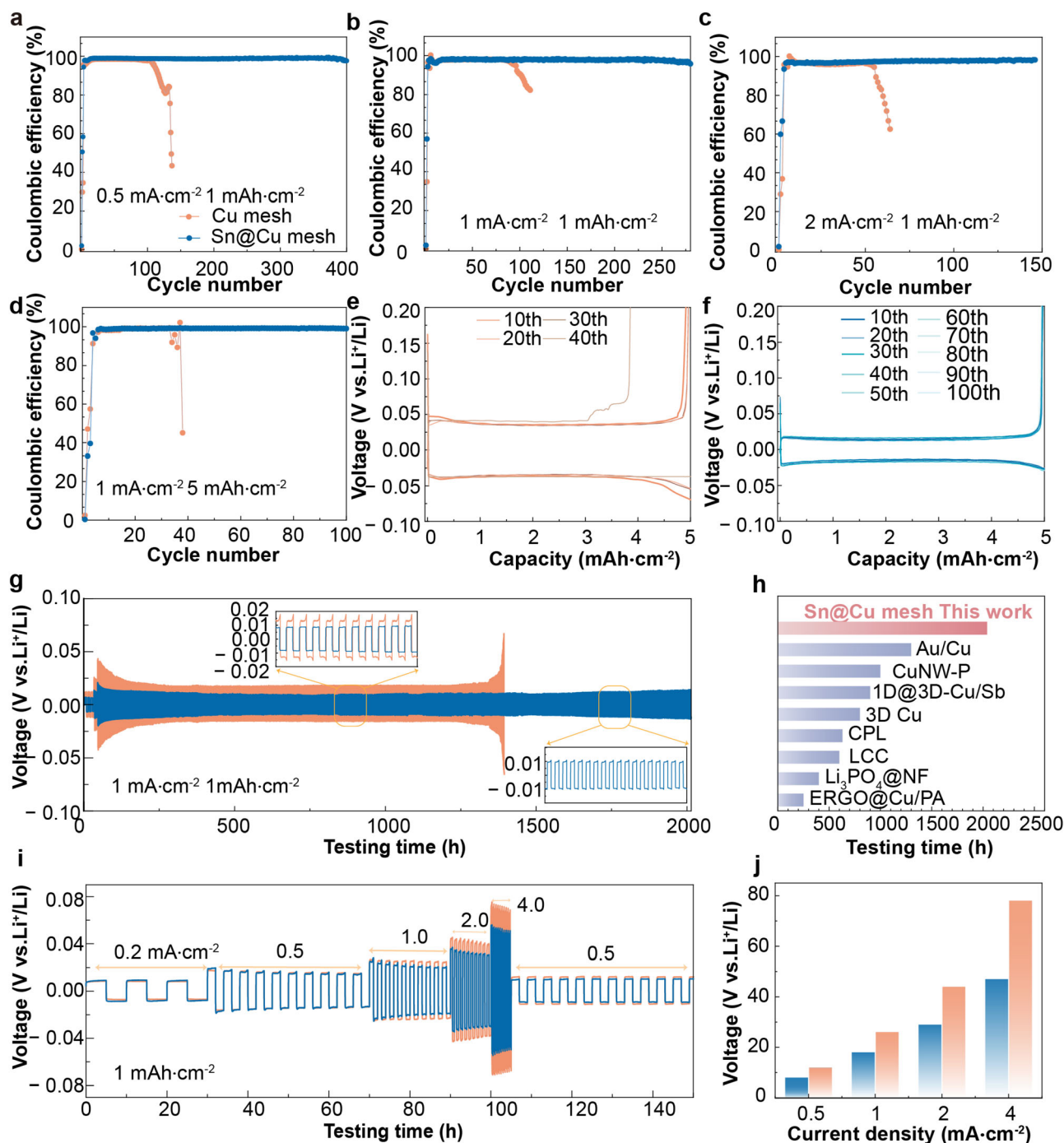


Fig. 5 CEs of Cu mesh and Sn@Cu mesh at current densities of **a** $0.5 \text{ mA}\cdot\text{cm}^{-2}$, **b** $1 \text{ mA}\cdot\text{cm}^{-2}$ and **c** $2 \text{ mA}\cdot\text{cm}^{-2}$ with capacity of $1 \text{ mAh}\cdot\text{cm}^{-2}$; **d** CEs of Cu mesh and Sn@Cu mesh at current density of $1 \text{ mA}\cdot\text{cm}^{-2}$ and capacity of $1 \text{ mAh}\cdot\text{cm}^{-2}$; voltage-capacity curves of **e** Cu mesh and **f** Sn@Cu mesh at different cycles; **g** galvanostatic cycling performance of Cu mesh and Sn@Cu mesh anodes in symmetric cells at current density of $0.5 \text{ mA}\cdot\text{cm}^{-2}$ and capacity of $1 \text{ mAh}\cdot\text{cm}^{-2}$; **h** comparison of cycle time at current density of $1 \text{ mA}\cdot\text{cm}^{-2}$ and capacity of $1 \text{ mAh}\cdot\text{cm}^{-2}$; **i** rate performance and **j** voltage of cells using different electrodes at a fixed capacity of $1 \text{ mAh}\cdot\text{cm}^{-2}$

(ACE) of 98.6% over 400 cycles in Fig. 5a at 0.5 and $1.0 \text{ mA}\cdot\text{cm}^{-2}$, far exceeding that of the Cu mesh, which achieves only 110 cycles. When the current density increases to 1.0 and $2.0 \text{ mA}\cdot\text{cm}^{-2}$ (Fig. 5b, c), the Sn@Cu

mesh maintains ACE at approximately 98.0% and 97.5% over 280 and 150 cycles, respectively. Contrastingly, the Cu mesh struggles to endure beyond 80 and 50 cycles at the respective rates. The charge–discharge curves in Fig. S13

indicate lower polarization in Sn@Cu mesh compared to Cu mesh. SEM images after 50 cycles (Fig. S14) reveal alarming holes and cracks in the Li-deposited surface of the Cu mesh, while Sn@Cu mesh maintains deposition with larger particles. Remarkably, at a current density of $1.0 \text{ mA}\cdot\text{cm}^{-2}$ and capacity of $5.0 \text{ mAh}\cdot\text{cm}^{-2}$, the Sn@Cu mesh electrode outperforms the Cu mesh electrode, achieving a remarkable 100 cycles with a Coulombic efficiency of 99.2% (Fig. 5d), compared with the 40 cycles of the Cu mesh electrode. The Sn@Cu mesh electrode also exhibits superior stability in polarization voltage throughout the cycling process (Fig. 5e, f). Even at $2.0 \text{ mA}\cdot\text{cm}^{-2}$, it maintains a stable cycling performance for 80 cycles (Fig. S15). The Sn@Cu mesh electrode exhibits excellent reversibility, effectively minimizing the loss of active Li. To investigate interfacial reactions, pre-deposited Sn@Cu mesh and Cu mesh electrodes with the Li pre-deposition of $10.0 \text{ mAh}\cdot\text{cm}^{-2}$ were utilized for assembling symmetrical cell. Figure 5g reveals a notable polarization voltage increase in the Cu mesh electrode after 1400 h at 18 mV (Fig. S16), leading to battery failure. Surprisingly, the Sn@Cu mesh electrode demonstrates an extended cycling life of over 2000 h at an ultra-low polarization voltage of 10 mV (Figs. S16, S17), a highly competitive performance as depicted in Fig. 5h and Table S4. The battery rate performance of the Sn@Cu mesh electrode demonstrates sustained low polarization even at a current density of $4 \text{ mA}\cdot\text{cm}^{-2}$ (47 vs. 78 mV) in Figs. 5i, j, S18, S19. The Sn@Cu mesh effectively reduces local current density, thereby accelerating Li^+ transport [29, 62]. Electrochemical Impedance Spectroscopy (EIS) results (Figs. S20, S21, Table S3) reveal that after an initial 10 cycles, the values of solution resistance (R_S) and solid-state electrolyte interfacial resistance (R_{SEI}) for Cu mesh and Sn@Cu mesh with different cycle numbers are 1.560 versus 2.325 Ω and 1.937 versus 1.698 Ω , respectively. Following 100 cycles, the Sn@Cu mesh maintains nearly constant impedance values ($R_{SEI} = 0.174$, $R_{ct} = 2.779$), while the Cu mesh experiences a tenfold increase. The superior reaction kinetics of the Sn@Cu mesh electrode contribute to its enhanced stability compared to the Cu mesh. Further, the capacitance values measured constantly increase in the Cu mesh while they remain the same (within statistical error) in the case of the Sn@Cu mesh. This further implies that the lithium growth is uniform and repeatable on Sn@Cu mesh while dead lithium is accumulating on the bare Cu mesh.

To validate the application potential of Sn@Cu mesh, commercial high-loading LFP ($1.8 \text{ mAh}\cdot\text{cm}^{-2}$) and NCM523 ($1.5 \text{ mAh}\cdot\text{cm}^{-2}$) were paired with Cu mesh-Li and Sn@Cu mesh-Li in full cells. As shown in Fig. 6a, Sn@Cu mesh-Li||LFP and Cu mesh-Li||LFP (N/P: 5.6) exhibit comparable initial capacities (Fig. S22), while the

Sn@Cu mesh electrode shows lower polarization (53.6 mV) than the Cu mesh electrode (60.5 mV). The Sn@Cu mesh electrode demonstrates a stable cyclic capacity retention of 82.3% over 250 cycles at 0.5C ($1C = 150 \text{ mAh}\cdot\text{g}^{-1}$), with a CE approaching 100%. In contrast, the Cu mesh electrode experiences a sharp capacity decline after 150 cycles. This issue is further illustrated in the charge–discharge curves (Fig. S23). The rate performance test results of Sn@Cu mesh-Li||LFP and Cu mesh-Li||LFP are presented in Figs. 6b, S24. At 3C, the Sn@Cu mesh electrode achieves a capacity of $116.8 \text{ mAh}\cdot\text{g}^{-1}$, while the Cu mesh electrode only reaches $86.6 \text{ mAh}\cdot\text{g}^{-1}$. Additionally, under zero excess Li conditions (anode-free Li metal cell), Sn@Cu mesh maintains excellent comparable stability with Cu mesh (Figs. S25, S26). Assembled into a pouch cell with LFP (Figs. 6c, S27), the Sn@Cu mesh can power LED lights displaying the “WHU” pattern. The Sn@Cu mesh-Li||NCM523 cell (N/P: 6.25) stably cycles for nearly 150 cycles and maintains a capacity retention of 75% and a CE close to 100% at 1C. In contrast, in the carbonate-based electrolyte, the Cu mesh-Li||NCM523 cell exhibits capacity fluctuations after 80 cycles, and the capacity declines to 0 after 150 cycles. The 0.3 Ah Sn@Cu mesh||NCM523 anode-free Li metal pouch cell ($3.8 \text{ mAh}\cdot\text{cm}^{-2}$) [63] was assembled in accordance with the configuration shown in Figs. 6d, S28. Remarkably, the Sn@Cu mesh electrode demonstrated exceptional cycling stability, exceeding 40 cycles with a capacity of 53%, as depicted in Figs. 6f, S29. These outstanding results underscore the efficacy of Sn modification in inhibiting dendrite growth during cycling, thereby enhancing the cyclic stability of Li metal batteries.

4 Conclusion

In summary, we display a meter-scale Sn@Cu mesh, fabricated using a straightforward and scalable chemical Sn-plating method. The lithiophilic Sn modifications play a crucial role in inducing two-dimensional Li nucleation, while the electric field distribution within the Cu skeleton promotes Li inward growth. This synergy results in the formation of a uniform and dense Li plating on the Sn@Cu mesh. Thanks to these significant advancements, Li||Cu half-cells demonstrate a remarkable Coulombic efficiency of 99.2% over 100 cycles at a high areal capacity of $5 \text{ mAh}\cdot\text{cm}^{-2}$. The Sn@Cu mesh-Li||Sn@Cu mesh-Li symmetrical cells exhibit exceptional stability with only a 10 mV polarization, cycling uninterrupted for over 2000 h at current density of $1 \text{ mA}\cdot\text{cm}^{-2}$ and capacity of $1 \text{ mAh}\cdot\text{cm}^{-2}$. When coupled with the NCM523 cathode, the full battery showcases an impressive retention of 75% after 150 cycles at 1C. Even in the case of a large-sized Sn@Cu

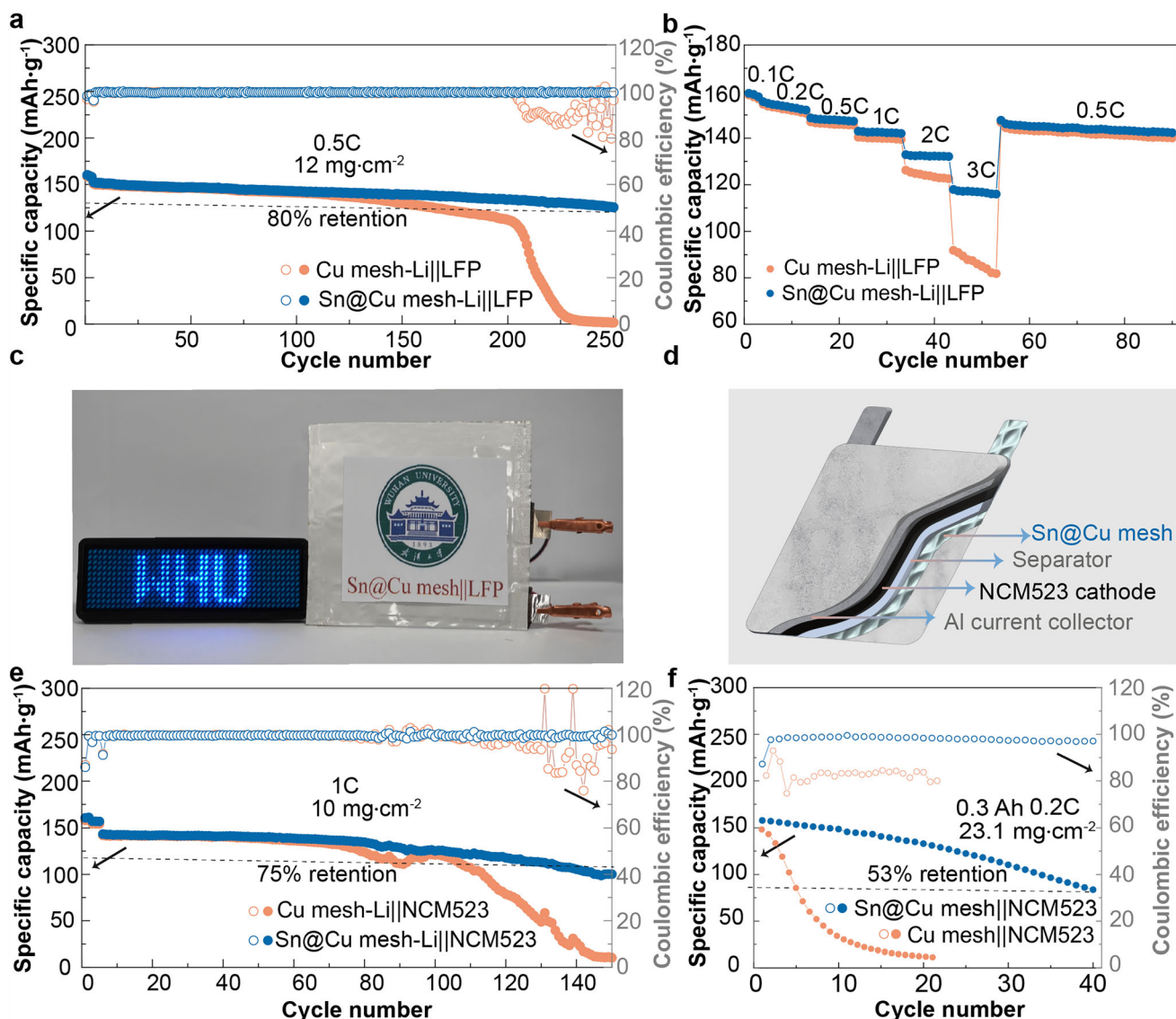


Fig. 6 **a** Long-term cycling stability of Cu mesh-Li||LFP, Sn@Cu mesh-Li||LFP full cells at 0.5C; **b** rate capability comparison of full batteries; **c** pouch cells light LED lights with word WHU; **d** schematic illustration of a Sn@Cu mesh||NCM523 pouch cell; **e** long-term cycling stability of Cu mesh-Li|| NCM523, Sn@Cu mesh-Li|| NCM523 full cells at 1C with 1 M LiPF₆ in EC/EMC/DMC (1:1:1 in vol%); **f** cycling performance of Cu mesh||NCM523 and Sn@Cu mesh||NCM523 pouch cell at 0.2C with 1 M LiPF₆ in EC/EMC/DMC (1:1:1 in vol%)

mesh||NCM523 anode-free pouch cell, it exhibits stable cycling performance, contrasting with the rapid capacity decay observed in batteries employing a Cu mesh electrode. Overall, the successful application of the roll-to-roll process in the fabrication of Sn@Cu mesh provides a pioneering strategy for the scalable production of current collectors in lithium metal batteries. These findings may also offer insights into the utilization of lithiophilic 3D current collectors in anode-free lithium metal batteries.

Acknowledgements This study was financially supported by the Key Research and Development Program of Hubei Province, China (No. 2023BAB108), the Natural Science Foundation of Hubei Province, China (No. 2022CFB096) and the National Natural Science

Foundation of China (Nos. 22279093 and 22075216). We would like to thank the Core Facility of Wuhan University and Shiyan Laboratory for access to analytical equipment.

Declarations

Conflict of interests The authors declare that they have no conflict of interest.

References

- [1] Chu S, Majumdar A. Opportunities and challenges for a sustainable energy future. *Nature*. 2012;488(7411):294. <https://doi.org/10.1038/nature11475>.



- [2] Shi P, Fu ZH, Zhou MY, Chen X, Yao N, Hou LP, Zhao CZ, Li BQ, Huang JQ, Zhang XQ, Zhang Q. Inhibiting intercrystalline reactions of anode with electrolytes for long-cycling lithium batteries. *Sci Adv.* 2022;8:eabq3445. <https://doi.org/10.1126/sciadv.abq3445>.
- [3] Zhang X, Yang YG, Zhou Z. Towards practical lithium-metal anodes. *Chem Soc Rev.* 2020;49(10):3040. <https://doi.org/10.1039/c9cs00838a>.
- [4] Yun QB, He YB, Lv W, Zhao Y, Li BH, Kang FY, Yang QH. Chemical dealloying derived 3D porous current collector for Li metal anodes. *Adv Mater.* 2016;28(32):6932. <https://doi.org/10.1002/adma.201601409>.
- [5] Yao LY, Hou LP, Song YW, Zhao M, Xie J, Li BQ, Zhang Q, Huang JQ, Zhang XQ. Recycling inactive lithium in lithium-sulfur batteries using organic polysulfide redox. *J Mater Chem A.* 2023;11(14):7441. <https://doi.org/10.1039/d3ta00096f>.
- [6] Park S, Jin HJ, Yun YS. Advances in the Design of 3D-structured electrode materials for lithium-metal anodes. *Adv Mater.* 2020;32(51):2002193. <https://doi.org/10.1002/adma.202002193>.
- [7] Wang M, Li Y, Li SY, Jia XX, Nie B, Sun HT, Wang YY, Zhu J. Lithiophilic montmorillonite as a robust substrate toward high-stable lithium metal anodes. *Rare Met.* 2023;42(7):2157. <https://doi.org/10.1007/s12598-022-02256-y>.
- [8] Qian JF, Henderson WA, Xu W, Bhattacharya P, Engelhard M, Borodin O, Zhang JG. High rate and stable cycling of lithium metal anode. *Nat Commun.* 2015;6(1):6362. <https://doi.org/10.1038/ncomms7362>.
- [9] Wu C, Zhou Y, Zhu XL, Zhan MZ, Yang HX, Qian JF. Research progress on high concentration electrolytes for Li metal batteries. *Acta Phys Chim Sin.* 2021;37(2):2008044. <https://doi.org/10.3866/pku.Whxb202008044>.
- [10] Wu ZC, Li RH, Zhang SQ, Lv L, Deng T, Zhang H, Zhang RX, Liu JJ, Ding SH, Fan LW, Chen LX, Fan XL. Deciphering and modulating energetics of solvation structure enables aggressive high-voltage chemistry of Li metal batteries. *Chem.* 2023;9(3):650. <https://doi.org/10.1016/j.chempr.2022.10.027>.
- [11] Hu AJ, Chen W, Du XC, Hu Y, Lei TY, Wang HB, Xue LX, Li YC, Sun H, Yan YC, Long JP, Shu CZ, Zhu J, Li BH, Wang XF, Xiong J. An artificial hybrid interphase for an ultrahigh-rate and practical lithium metal anode. *Energy Environ Sci.* 2021;14(7):4115. <https://doi.org/10.1039/d1ee00508a>.
- [12] Liu JF, Wu ZY, Stadler FJ, Huang YF. High dielectric poly(vinylidene fluoride)-based polymer enables uniform lithium-ion transport in solid-state ionogel electrolytes. *Angew Chem Int Ed.* 2023;62(26):e202300243. <https://doi.org/10.1002/anie.202300243>.
- [13] Wu Q, Fang MD, Jiao SZ, Li SY, Zhang SC, Shen ZY, Mao SL, Mao JL, Zhang JH, Tan YZ, Shen K, Lv JX, Hu W, He Y, Lu YY. Phase regulation enabling dense polymer-based composite electrolytes for solid-state lithium metal batteries. *Nat Commun.* 2023;14(1):6296. <https://doi.org/10.1038/s41467-023-41808-3>.
- [14] Yue LG, Wang XY, Chen L, Shen DJ, Shao ZH, Wu H, Xiao SF, Liang WQ, Yu YJ, Li YY. In situ interface engineering of highly nitrogen-rich triazine-based covalent organic frameworks for an ultra-stable, dendrite-free lithium-metal anode. *Energy Environ Sci.* 2024;17(3):1117. <https://doi.org/10.1039/d3ee02803h>.
- [15] Zhang CH, Xie JY, Zhao CT, Yang YX, An Q, Mei ZY, Xu QJ, Ding YQ, Zhao GF, Guo H. Regulating the lithium ions' local coordination environment through designing a COF with single atomic Co site to achieve dendrite-free lithium-metal batteries. *Adv Mater.* 2023;35(40):2304511. <https://doi.org/10.1002/adma.202304511>.
- [16] Li WH, Quirk JA, Li MS, Xia W, Morgan LM, Yin W, Zheng M, Gallington LC, Ren Y, Zhu N, King G, Feng RF, Li RY, Dawson JA, Sham TK, Sun XL. Precise tailoring of lithium-ion transport for ultralong-cycling dendrite-free all-solid-state lithium metal batteries. *Adv Mater.* 2023;36:2302647. <https://doi.org/10.1002/adma.202302647>.
- [17] Alexander GV, Shi C, O'Neill J, Wachsman ED. Extreme lithium-metal cycling enabled by a mixed ion- and electron-conducting garnet three-dimensional architecture. *Nat Mater.* 2023;22(9):1136. <https://doi.org/10.1038/s41563-023-01627-9>.
- [18] Wang ZY, Xia JL, Ji X, Liu YJ, Zhang JX, He XZ, Zhang WR, Wan HL, Wang CS. Lithium anode interlayer design for all-solid-state lithium-metal batteries. *Nat Energy.* 2024;9:251. <https://doi.org/10.1038/s41560-023-01426-1>.
- [19] Yang CP, Yin YX, Zhang SF, Li NW, Guo YG. Accommodating lithium into 3D current collectors with a submicron skeleton towards long-life lithium metal anodes. *Nat Commun.* 2015;6(1):8058. <https://doi.org/10.1038/ncomms9058>.
- [20] Wang YN, Zhan YX, Zhang XQ, Huang JQ. Advances in carbon-based composite anodes with gradients of lithiophilicity and conductivity used for stable lithium metal batteries. *New Carbon Mater.* 2023;38(4):623. [https://doi.org/10.1016/s1872-5805\(23\)60744-9](https://doi.org/10.1016/s1872-5805(23)60744-9).
- [21] Zhou B, Bonakdarpour A, Stoševski I, Fang B, Wilkinson DP. Modification of Cu current collectors for lithium metal batteries—a review. *Prog Mater Sci.* 2022;130:100996. <https://doi.org/10.1016/j.pmatsci.2022.100996>.
- [22] Ye SF, Chen XJ, Zhang R, Jiang Y, Huang FY, Huang HJ, Yao Y, Jiao SH, Chen X, Zhang Q, Yu Y. Revisiting the role of physical confinement and chemical regulation of 3D hosts for dendrite-free Li metal anode. *Nano-Micro Lett.* 2022;14(1):187. <https://doi.org/10.1007/s40820-022-00932-3>.
- [23] Zheng GY, Lee SW, Liang Z, Lee H, Yan K, Yao HB, Wang HT, Li WY, Chu S, Cui Y. Interconnected hollow carbon nanospheres for stable lithium metal anodes. *Nat Nanotechnol.* 2014;9(8):618. <https://doi.org/10.1038/nnano.2014.152>.
- [24] Zhang W, Liang HC, Zhu KR, Tian Y, Liu Y, Chen JY, Li W. Three-dimensional macro/mesoporous C-TiC nanocomposites for dendrite-free lithium metal anode. *Acta Phys Chim Sin.* 2022;38(6):2105024. <https://doi.org/10.3866/pku.Whxb202105024>.
- [25] Kwon H, Lee JH, Roh Y, Baek J, Shin DJ, Yoon JK, Ha HJ, Kim JY, Kim HT. An electron-deficient carbon current collector for anode-free Li-metal batteries. *Nat Commun.* 2021;12(1):5537. <https://doi.org/10.1038/s41467-021-25848-1>.
- [26] Wang YL, Shen YB, Du ZL, Zhang XF, Wang K, Zhang HY, Kang T, Guo F, Liu CH, Wu XD, Lu W, Chen LW. A lithium-carbon nanotube composite for stable lithium anodes. *J Mater Chem A.* 2017;5(45):23434. <https://doi.org/10.1039/c7ta08531a>.
- [27] Zuo TT, Yin YX, Wang SH, Wang PF, Yang XN, Liu J, Yang CP, Guo YG. Trapping lithium into hollow silica microspheres with a carbon nanotube core for dendrite-free lithium metal anodes. *Nano Lett.* 2018;18(1):297. <https://doi.org/10.1021/acs.nanolett.7b04136>.
- [28] Lu ZT, Liu SH, Li CF, Huang JL, Wu DC, Fu RW. 3D porous carbon networks with highly dispersed SiO_x by molecular-scale engineering toward stable lithium metal anodes. *Chem Commun.* 2019;55(43):6034. <https://doi.org/10.1039/c9cc01927h>.
- [29] Li Q, Zhu SP, Lu YY. 3D porous Cu current collector/Li-metal composite anode for stable lithium-metal batteries. *Adv Funct Mater.* 2017;27(18):1606422. <https://doi.org/10.1002/adfm.201606422>.
- [30] Yang I, Jeong J, Seok JY, Kim S. Structurally tailored hierarchical Cu current collector with selective inward growth of lithium for high-performance lithium metal batteries. *Adv Energy Mater.* 2022;13(2):2202321. <https://doi.org/10.1002/aenm.202202321>.
- [31] Ingber TTK, Bela MM, Püttmann F, Dohmann JF, Bieker P, Börner M, Winter M, Stan MC. Elucidating the lithium deposition behavior in open-porous copper micro-foam negative electrodes for zero-excess lithium metal batteries. *J Mater Chem A.* 2023;11(33):17828. <https://doi.org/10.1039/d3ta04060g>.

- [32] Liao JL, Zhang S, Bai TS, Ji FJ, Li DP, Cheng J, Zhang HQ, Lu JY, Gao Q, Ci LJ. A ZnO decorated 3D copper foam as a lithiophilic host to construct composite lithium metal anodes for Li–O₂ batteries. *Rare Met.* 2023;42(6):1969. <https://doi.org/10.1007/s12598-023-02281-5>.
- [33] Park SK, Copic D, Zhao TZ, Rutkowska A, Wen B, Sanders K, He R, Kim H-K, De Volder M. 3D porous Cu-composites for stable Li-metal battery anodes. *ACS Nano.* 2023;17(15):14658. <https://doi.org/10.1021/acsnano.3c02223>.
- [34] Chen JX, Zhang GQ, Qin XY, Lin K, Yang ZJ, Liang GM, Xia Y, Zhang GB, Wu HK, Cai QC, Lin H, Li BH. Lithium-induced graphene layer containing Li₃P alloy phase to achieve ultra-stable electrode interface for lithium metal anode. *Rare Met.* 2023. <https://doi.org/10.1007/s12598-023-02433-7>.
- [35] Fei XY, Gao H, Xu YZ, Ma WS, Yu B, Tan FQ, Cheng GH, Zhang ZH. Porous lithiophilic Cu-Sn solid solution current collector for dendrite-free lithium metal batteries. *Energy Storage Mater.* 2024; 65:103079. <https://doi.org/10.1016/j.ensm.2023.103079>.
- [36] Zhang B, Ma JP, Zhao Y, Li T, Yang JL, Zhang ZL, Wei SZ, Zhou GM. Design and application of copper/lithium composite anodes for advanced lithium metal batteries. *Rare Met.* 2023; 43(3):942. <https://doi.org/10.1007/s12598-023-02477-9>.
- [37] Li YH, Li Y, Zhang LL, Tao HC, Li QY, Zhang JJ, Yang XL. Lithiophilicity: the key to efficient lithium metal anodes for lithium batteries. *J Energy Chem.* 2023;77:123. <https://doi.org/10.1016/j.jechem.2022.10.026>.
- [38] Yan K, Lu ZD, Lee H, Xiong F, Hsu P, Li Y, Zhao J, Chu S, Cui Y. Selective deposition and stable encapsulation of lithium through heterogeneous seeded growth. *Nat Energy.* 2016;1(3):1. <https://doi.org/10.1038/nenergy.2016.10>.
- [39] Liu JX, Pei NB, Yang XY, Li RY, Hua HM, Zhang P, Zhao JB. Recent advances in lithiophilic materials: material design and prospects for lithium metal anode application. *Energy Mater.* 2023;3:300024. <https://doi.org/10.20517/energymater.2023.08>.
- [40] Liao YQ, Yuan LX, Xiang JW, Zhang W, Cheng ZX, He B, Li Z, Huang YH. Realizing both high gravimetric and volumetric capacities in Li/3D carbon composite anode. *Nano Energy.* 2020;69:104471. <https://doi.org/10.1016/j.nanoen.2020.104471>.
- [41] Zhang S, Xiao SY, Li DP, Liao JL, Ji FJ, Liu HB, Ci LJ. Commercial carbon cloth: an emerging substrate for practical lithium metal batteries. *Energy Storage Mater.* 2022;48:172. <https://doi.org/10.1016/j.ensm.2022.03.014>.
- [42] Chen JY, Wang YZ, Li SJ, Chen HR, Qiao X, Zhao J, Ma Y, Alshareef HN. Porous metal current collectors for alkali metal batteries. *Adv Sci.* 2022;10(1):e2205695. <https://doi.org/10.1002/advs.202205695>.
- [43] Wu Q, Qin MS, Yan H, Zhong W, Zhang W, Liu MC, Cheng SJ, Xie J. Facile replacement reaction enables nano-Ag-decorated three-dimensional Cu foam as high-rate lithium metal anode. *ACS Appl Mater Interfaces.* 2022;14(37):42030. <https://doi.org/10.1021/acsaami.2c10920>.
- [44] Luan JY, Zhang Q, Yuan HY, Peng ZG, Tang YG, Wu SG, Wang HY. Sn layer decorated copper mesh with superior lithiophilicity for stable lithium metal anode. *Chem Eng J.* 2020; 395:124922. <https://doi.org/10.1016/j.cej.2020.124922>.
- [45] Zhao J, Li N, Cui GF, Zhao JW. Study on immersion tin process by electrochemical methods and molecular orbital theory. *J Electrochem Soc.* 2006;153:C848. <https://doi.org/10.1149/1.2358119>.
- [46] Luo Z, Liu C, Tian Y, Zhang Y, Jiang YL, Hu JH, Hou HS, Zou GQ, Ji XB. Dendrite-free lithium metal anode with lithiophilic interphase from hierarchical frameworks by tuned nucleation. *Energy Storage Mater.* 2020;27:124. <https://doi.org/10.1016/j.ensm.2020.01.025>.
- [47] Zhang HZ, Xu DY, Yang F, Xie JH, Liu QY, Liu DJ, Zhang MH, Lu XH, Meng YS. A high-capacity Sn metal anode for aqueous acidic batteries. *Joule.* 2023;7(5):971. <https://doi.org/10.1016/j.joule.2023.04.011>.
- [48] Luan JY, Zhang Q, Yuan HY, Sun D, Peng ZG, Tang YG, Ji XB, Wang HY. Plasma-strengthened lithiophilicity of copper oxide nanosheet-decorated Cu foil for stable lithium metal anode. *Adv Sci.* 2019;6(20):1901433. <https://doi.org/10.1002/advs.201901433>.
- [49] Ying HJ, Han WQ. Metallic Sn-based anode materials: application in high-performance lithium-ion and sodium-ion batteries. *Adv Sci.* 2017;4(11):1700298. <https://doi.org/10.1002/advs.201700298>.
- [50] Wang XC, He YF, Tu SB, Fu L, Chen ZH, Liu SY, Cai Z, Wang L, He XM, Sun YM. Li plating on alloy with superior electro-mechanical stability for high energy density anode-free batteries. *Energy Storage Mater.* 2022;49:135. <https://doi.org/10.1016/j.ensm.2022.04.009>.
- [51] Zhang LZ, Meng QK, Feng XP, Shen M, Zhang YQ, Zhuang QC, Zheng RG, Wang ZY, Cui YH, Sun HY, Liu YG. A lithium-tin fluoride anode enabled by ionic/electronic conductive paths for garnet-based solid-state lithium metal batteries. *Rare Met.* 2023; 43(2):575. <https://doi.org/10.1007/s12598-023-02468-w>.
- [52] Martin W, Besenhard JO. Electrochemical lithiation of tin and tin-based intermetallics and composites. *Electrochim Acta.* 1999; 45(1–2):31. [https://doi.org/10.1016/S0013-4686\(99\)00191-7](https://doi.org/10.1016/S0013-4686(99)00191-7).
- [53] Han QG, Yi Z, Cheng Y, Wu YM, Wang LM. Simple preparation of Cu₆Sn₅/Sn composites as anode materials for lithium-ion batteries. *RSC Adv.* 2016;6(19):15279. <https://doi.org/10.1039/c5ra23788b>.
- [54] Shen XJ, Zhao GG, Yu XB, Huang HH, Wang M, Zhang NP. Multifunctional SnSe–C composite modified 3D scaffolds to regulate lithium nucleation and fast transport for dendrite-free lithium metal anodes. *J Mater Chem A.* 2021;9(38):21695. <https://doi.org/10.1039/d1ta06836a>.
- [55] Anantharaj S, Noda S, Driess M, Menezes PW. The pitfalls of using potentiodynamic polarization curves for tafel analysis in electrocatalytic water splitting. *ACS Energy Lett.* 2021;6:1607. <https://doi.org/10.1021/acsaenergylett.1c00608>.
- [56] Zou PC, Wang Y, Chiang SW, Wang XY, Kang FY, Yang C. Directing lateral growth of lithium dendrites in micro-compartmented anode arrays for safe lithium metal batteries. *Nat Commun.* 2018;9(1):464. <https://doi.org/10.1038/s41467-018-02888-8>.
- [57] Thirumalraj B, Hagos TT, Huang CJ, Teshager MA, Cheng JH, Su WN, Hwang BJ. Nucleation and growth mechanism of lithium metal electroplating. *J Am Chem Soc.* 2019;141(46): 18612. <https://doi.org/10.1021/jacs.9b10195>.
- [58] Zhang J, Yue XY, Wu ZY, Chen YM, Bai Y, Sun KN, Wang ZH, Liang Z. A LiF-rich solid electrolyte interphase in a routine carbonate electrolyte by tuning the interfacial chemistry behavior of LiPF₆ for stable Li metal anodes. *Nano Lett.* 2023; 23(20):9609. <https://doi.org/10.1021/acs.nanolett.3c03340>.
- [59] Li ZJ, Zhou YC, Wang Y, Lu YC. Solvent-mediated Li₂S electrodeposition: a critical manipulator in lithium–sulfur batteries. *Adv Energy Mater.* 2018;9(1):1802207. <https://doi.org/10.1002/aenm.201802207>.
- [60] Mamme MH, Kohn C, Deconinck J, Ustarroz J. Numerical insights into the early stages of nanoscale electrodeposition: nanocluster surface diffusion and aggregative growth. *Nanoscale.* 2018;10(15):7194. <https://doi.org/10.1039/c7nr08529j>.
- [61] Bewick A, Fleischmann M, Thirsk HR. Kinetics of the electrocrystallization of thin films of calomel. *Trans Faraday Soc.* 1962;58:2200. <https://doi.org/10.1039/TF9625802200>.
- [62] Dong QJ, Zhang WX, Gao M, Zhang SY, Liu Y, Sun ZY, Chen Q, Wang JJ, Han XP, Hu WB. Rapid synthesis of large-area and integrated anode current collector via electroless in-situ Sn



- modification strategy for lithium metal batteries. *Chem Eng J.* 2023;471:144483. <https://doi.org/10.1016/j.cej.2023.144483>.
- [63] Qian JF, Adams BD, Zheng JM, Xu W, Henderson WA, Wang J, Bowden ME, Xu SC, Hu JZ, Zhang JG. Anode-free rechargeable lithium metal batteries. *Adv Funct Mater.* 2016;26(39):7094. <https://doi.org/10.1002/adfm.201602353>.

Springer Nature or its licensor (e.g. a society or other partner) holds exclusive rights to this article under a publishing agreement with the author(s) or other rightsholder(s); author self-archiving of the accepted manuscript version of this article is solely governed by the terms of such publishing agreement and applicable law.